Absence of E_{2g} Nematic Instability and Dominant A_{1g} Response in the Kagome Metal CsV$_3$Sb$_5$

Zhaoyu Liu[1,*] Yue Shi,[2] Qianni Jiang,[1] Elliott W. Rosenberg,[1] Jonathan M. DeStefano,[1] Jinjin Liu,[3,4]
Chaowei Hu,[1] Yuzhou Zhao,[1,2] Zhiwei Wang,[3,4] Yugui Yao,[3,4] David Graf,[5]
Pengcheng Dai,[6] Jihui Yang,[2] Xiaodong Xu,[1,2] and Jiun-Haw Chu[1,†]

[1]*Department of Physics, University of Washington, Seattle, Washington 98195, USA*
[2]*Department of Materials Science and Engineering, University of Washington,
Seattle, Washington 98195, USA*
[3]*Centre for Quantum Physics, Key Laboratory of Advanced Optoelectronic Quantum Architecture and
Measurement (MOE), School of Physics, Beijing Institute of Technology, Beijing 100081, China*
[4]*Beijing Key Lab of Nanophotonics and Ultrafine Optoelectronic Systems,
Beijing Institute of Technology, Beijing 100081, China*
[5]*National High Magnetic Field Laboratory, Florida State University, Tallahassee, Florida 32306, USA*
[6]*Department of Physics and Astronomy, Rice University, Houston, Texas 77005, USA*

Ever since the discovery of the charge density wave (CDW) transition in the kagome metal CsV$_3$Sb$_5$, the nature of its symmetry breaking has been under intense debate. While evidence suggests that the rotational symmetry is already broken at the CDW transition temperature (T_{CDW}), an additional electronic nematic instability well below T_{CDW} has been reported based on the diverging elastoresistivity coefficient in the anisotropic channel ($m_{E_{2g}}$). Verifying the existence of a nematic transition below T_{CDW} is not only critical for establishing the correct description of the CDW order parameter, but also important for understanding low-temperature superconductivity. Here, we report elastoresistivity measurements of CsV$_3$Sb$_5$ using three different techniques probing both isotropic and anisotropic symmetry channels. Contrary to previous reports, we find the anisotropic elastoresistivity coefficient $m_{E_{2g}}$ is temperature independent, except for a step jump at T_{CDW}. The absence of nematic fluctuations is further substantiated by measurements of the elastocaloric effect, which show no enhancement associated with nematic susceptibility. On the other hand, the symmetric elastoresistivity coefficient $m_{A_{1g}}$ increases below T_{CDW}, reaching a peak value of 90 at $T^* = 20$ K. Our results strongly indicate that the phase transition at T^* is not nematic in nature and the previously reported diverging elastoresistivity is due to the contamination from the A_{1g} channel.

I. INTRODUCTION

Kagome metals have emerged as a new platform to investigate the interplay between topology and correlation owing to their unique lattice structures [1]. The frustrated corner-sharing triangular lattice naturally gives rise to electronic structures with flat bands, van Hove singularities, and Dirac crossings [2]. Several interesting phenomena have been discovered in kagome metals, including the giant anomalous Hall effect (AHE) in Weyl semimetal Co$_3$Sn$_2$S$_2$ [3], massive Dirac fermions in Fe$_3$Sn$_2$ [4], and

charge density wave (CDW) order in FeGe, ScV$_6$Sn$_6$, and the AV$_3$Sb$_5$ (A = K, Rb, Cs) family [5–7]. Among the kagome metals, the AV$_3$Sb$_5$ (A = K, Rb, Cs) family has attracted significant attention due to the exotic behavior of its CDW phase ($T_{CDW} = 78$–104 K) and superconducting phase ($T_c = 1$–3 K) [7–18]. In particular, the nature of the symmetry breaking in the CDW phase is not yet settled despite extensive investigations. Early studies including the measurements of AHE, optical Kerr effect, and change of muon relaxation rate all suggested that time-reversal symmetry is broken in the CDW phase [19–26], raising the intriguing possibility that the CDW is a form of loop current order [27,28]. Nevertheless, these observations are challenged by the most recent measurement of the high-resolution polar Kerr effect, which found no observable Kerr response in zero field [29,30]. Therefore, whether time-reversal symmetry is truly broken remains an open question.

*Contact author: zhyliu@uw.edu
†Contact author: jhchu@uw.edu

In addition to time-reversal symmetry, the rotational symmetry in the CDW phase has also been intensely studied. A twofold anisotropy in the CDW phase that breaks the C_6 rotational symmetry was first reported by angle-dependent magnetoresistance measurements [31]. Further studies including scanning tunneling spectroscopy (STM) [32,33], Raman spectroscopy [34,35], optical bire-fringence measurements [22,36], and angle-resolved photo-emission spectroscopy [37–39], all confirmed the observed twofold anisotropy. However, the temperature at which rotational symmetry is broken remains a key question. While most studies agree that the breaking of rotational symmetry happens at T_{CDW}, a diverging elastoresistivity response was reported within the CDW phase [40,41], which was argued as evidence for an electronic nematic instability well below T_{CDW}.

The electronic nematic phase refers to a spontaneous rotational-symmetry-breaking phase while preserving translational symmetry, which has been extensively studied in strongly correlated electronic systems [42,43]. In the context of an Fe-based superconductor [44–47], nematicity is understood as a vestigial order of the underlying spin density wave or CDW phases [43,48–50]. The partial melting of the density waves destroys long-range perio-dicity while continuing to break rotational symmetry; hence, the nematic transition is always above the density wave transition in these materials. A salient feature of the nematicity is a diverging nematic susceptibility at temper-atures above the phase transition, which can be probed by elastoresistivity measurements, where resistivity anisotropy serves as a proxy for the nematic order parameter and the anisotropic strain serves as its conjugate field. For instance, a diverging elastoresistivity coefficient in the anisotropic strain channel ($m_{B_{2g}}$) with a Curie-Weiss temperature dependence was observed above the nematic transition in $Ba(Fe_{1-x}Co_x)_2As_2$ [44].

In this context, a diverging elastoresistivity in CsV_3Sb_5 that peaks at $T^* \approx 35$ K, a temperature well below T_{CDW}, is rather unusual [40]. It would imply the rotational symmetry is not broken at T_{CDW}, which is inconsistent with the majority of previous experimental observations [22,33,36]. Another possible explanation is that the rotational sym-metry is only weakly broken at T_{CDW} by the π phase shift of the CDW order between different kagome layers [51], while the CDW within the two-dimensional kagome plane remains isotropic. At a lower temperature T^*, the rotational symmetry within the kagome plane is broken, leading to diverging elastoresistivity [52]. In either scenario, the existence of a nematic instability below T_{CDW} provides strong constraints to distinguish between various proposals for the CDW order parameter [17,28,51–55]. In addition, a very recent elastoresistivity study proposed a nematic quantum critical point residing within the first supercon-ducting dome in the phase diagram of Ti-doped CsV_3Sb_5 [41], which was argued as evidence for nematic fluctuation-

enhanced superconducting pairing. On the other hand, it has been shown that nonideal experiment configura-tions, such as what is incorporated in the differential elastoresistivity technique used in Refs. [40,41], may lead to the mixing of elastoresistivity signals in different symmetry channels, resulting in a false diverging nematic response even though the leading instability is in other symmetry channels [56–59]. The purpose of this work is to perform a comprehensive study of elastoresistivity and the elastocaloric effect in CsV_3Sb_5 to elucidate the symmetry associated with the proposed transition at T^*.

II. RESULTS

A. Electrical transport characterization

CsV_3Sb_5 single crystals have a hexagonal shape with the a axis along the natural growth edges, consistent with the sixfold rotational symmetry of the kagome lattice [Fig. 1(a)]. The CDW transition occurs at $T_{CDW} = 94$ K, which can be seen from a resistivity anomaly and a sharp peak in $d\rho/dT$ as shown in Fig. 1(b). The superconducting transition is at $T_c = 3$ K. The residual resistivity ratio of $\rho(300 \text{ K})/\rho(5 \text{ K}) = 143.5$ indicates the high quality of the single crystals. The AHE is observed in the in-plane Hall resistivity below T_{CDW} [Fig. 1(c)], consistent with previous experiments [20]. The Shubnikov–de Haas quantum oscil-lations can be observed in longitudinal resistivity below 30 K [Fig. 1(d)]. The oscillatory component $\Delta\rho_{xx}$ as a function of inverse field and its fast Fourier transform are shown in Figs. 1(e) and 1(f), respectively. Four principal frequencies at 11, 28, 73, and 90 T were observed in the low-frequency regime (with some high-frequency peaks not shown here) in high field measurements up to 35 T. These observations are all in agreement with previous reports, providing a solid foundation to further study the elastoresponse in these single crystals [20,60,61].

B. Elastoresistivity

Elastoresistivity is a fourth-rank symmetric tensor that relates the change of resistivity of a system to the externally induced strains. When using Voigt notation, the elastor-esistivity tensor can be expressed as a second-rank 6×6 tensor:

$$m_{ij} = \frac{\partial(\Delta\rho/\rho)_i}{\partial\varepsilon_j}, \qquad (1)$$

where the indices i, $j = 1$–6 represent $1 = xx$, $2 = yy$, etc. [45]. These elastoresistivity coefficients can be further grouped into different symmetry channels based on the irreducible representations of the point group of the crystal lattice. For example, in D_{6h}, the elastoresistivity coefficients associated with the isotropic A_{1g} irrep and the anisotropic E_{2g} irrep are $m_{A_{1g}} = m_{11} + m_{12} - m_{13}[2\nu_{ac}/(1 - \nu_{ab})]$ and $m_{E_{2g}} = m_{11} - m_{12}$, respectively.
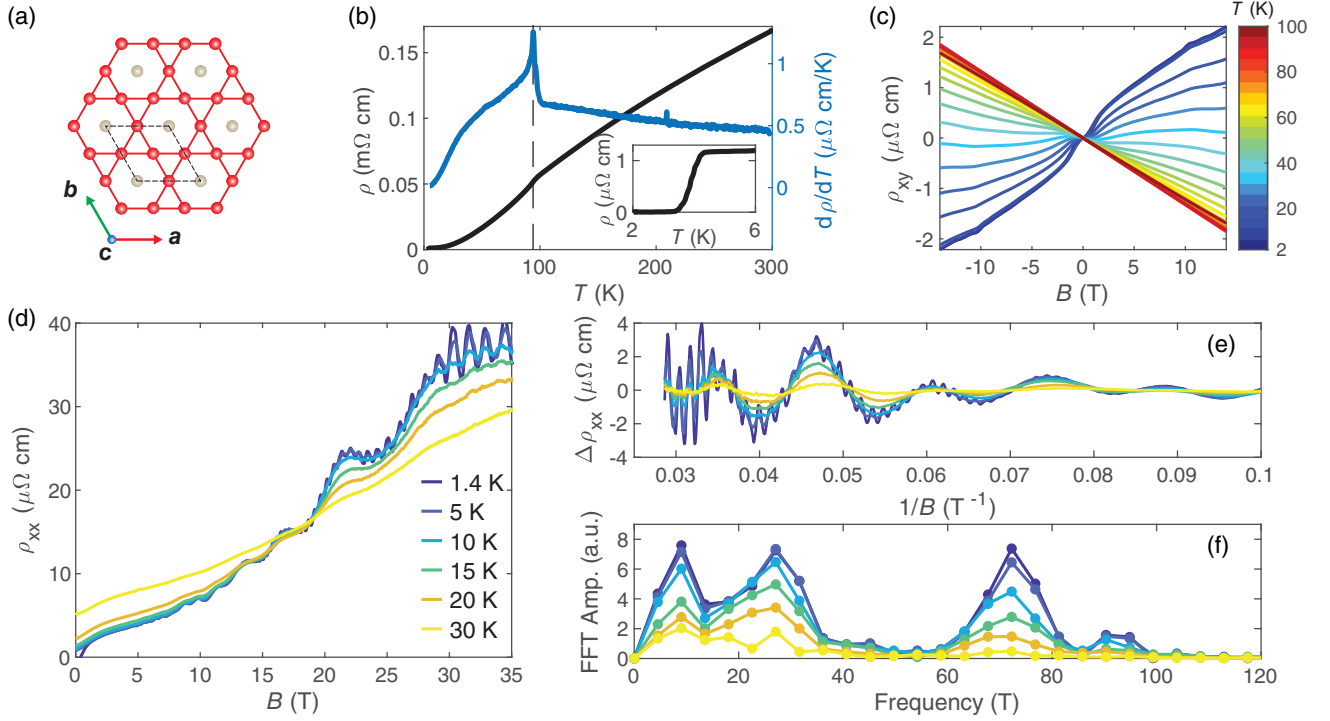
FIG. 1. Electric transport characterization of CsV_3Sb_5. (a) In-plane kagome net composed of vanadium atoms with antimony atoms filled in the center of the hexagonal lattice. (b) Temperature dependence of in-plane resistivity and its first derivative. The CDW transition temperature $T_{CDW} = 94$ K is shown as a vertical dashed line. The inset shows the superconducting transition at 4 K. The residual resistivity ratio is 143.5. (c) Magnetic field dependence of Hall resistivity at different temperatures with the field direction along the c axis. (d) Magnetoresistance below 30 K. (e) The polynomial background-subtracted magnetoresistance in (d) plotted as a function of the inverse magnetic field. (f) The fast Fourier transform of the quantum oscillations in (e).

Here, the $\nu_{ab,ac}$ are the in-plane and out-of-plane Poisson ratios (see Sec. V) [40,62]. In a material with an electronic nematic instability, the diverging susceptibility associated with the nematic transition will manifest in a diverging temperature dependence of the elastoresistivity coefficient in the anisotropic symmetry channel.

When measuring elastoresistivity, single crystals are glued on the sidewall of a piezostack, which induces a combination of purely anisotropic strain $\frac{1}{2}(\varepsilon_{xx} - \varepsilon_{yy})$ and isotropic strain $\frac{1}{2}(\varepsilon_{xx} + \varepsilon_{yy})$ when an external voltage is applied to the stack. In order to separate the isotropic and anisotropic symmetry channels, both ρ_{xx} and ρ_{yy} need to be measured. Three experimental techniques have been developed to measure elastoresistivity coefficients. The first technique that was developed is the differential elastoresistivity technique [44], which measures ρ_{xx} and ρ_{yy} using two separate bar-shaped samples cut along the same crystal axes but oriented perpendicularly on the stack, as shown in the top configuration in Fig. 2(a). However, it was soon realized that this technique inevitably introduces cross-contamination between different symmetry channels [56,57]. Exact symmetry decomposition requires identical strain transmission in both samples, which is never the case in any practical experiment. In fact, the bar-shaped

sample results in more effective strain transmission for the uniaxial strain along the bar direction. Therefore, a bar-shaped sample glued along the x (y) direction experiences dominantly uniaxial strain ε_{xx} (ε_{yy}) even though nominally the same anisotropic strain $\varepsilon_{xx} - \varepsilon_{yy}$ was applied. To address this issue, the modified Montgomery technique [45] and the transverse method [63] were subsequently developed. The modified Montgomery technique allows for obtaining ρ_{xx} and ρ_{yy} using a single square sample [middle configuration in Fig. 2(a)], and the transverse technique enables the direct measurement of the resistivity anisotropy $\rho_{x'y'}$ in a five-contact bar-shaped sample (bottom configuration; see details in Sec. V). Both methods measure the full resistivity tensors from the same single crystalline samples; hence, they do not suffer cross-contamination issues, and the symmetry decomposition is exact.

To thoroughly examine the elastoresistivity coefficients of CsV_3Sb_5, all three techniques mentioned above were employed. We found that resistivity as a function of strain is linear in both E_{2g} and A_{1g} symmetry channels at all temperatures for all measurements [Figs. 2(b)–2(e)], with only weak hysteresis near T_{CDW} likely due to structural domains. This suggests that all the measured elastoresistivity coefficients are in the near-zero strain linear response
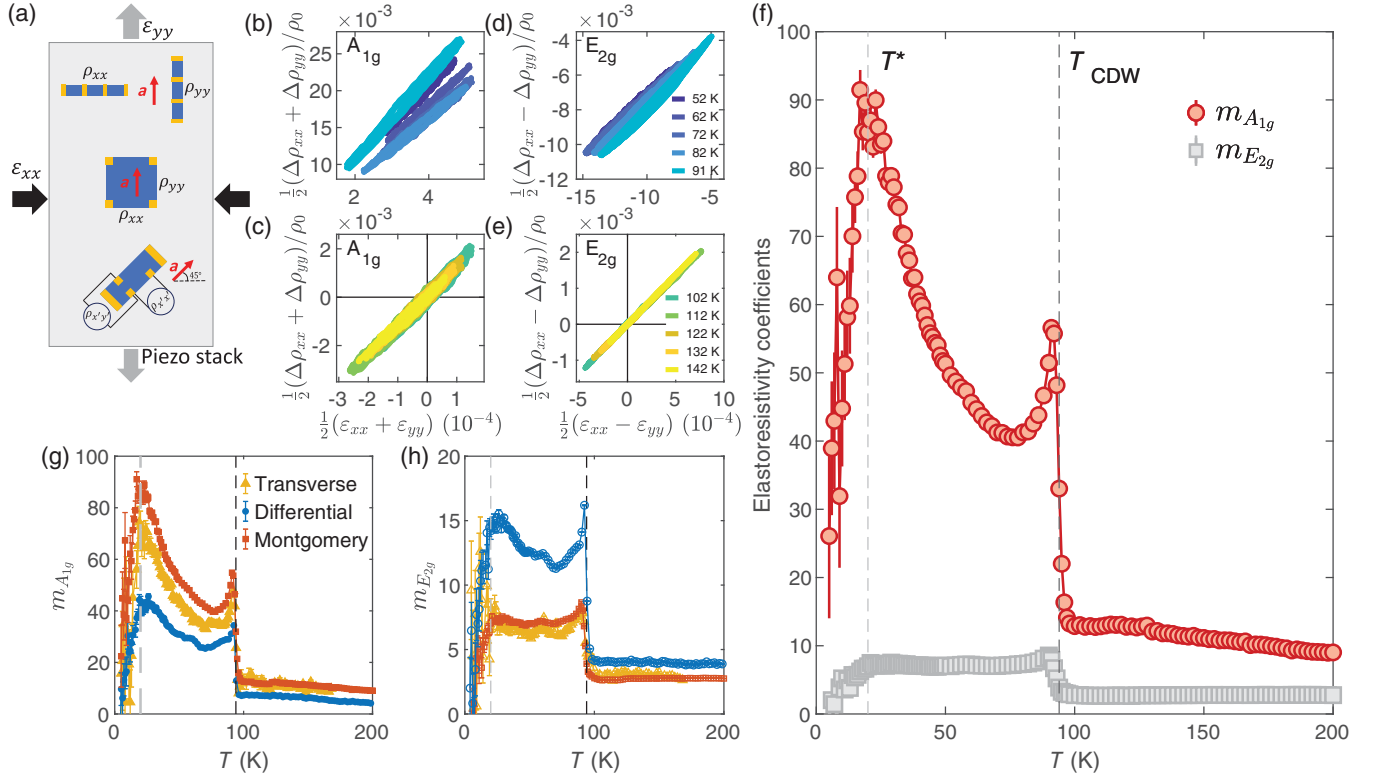
FIG. 2. Measurements of elastoresistivity coefficients in CsV_3Sb_5. (a) Schematic of three elastoresistivity measurement techniques. Samples are glued on the side wall of a piezostack (gray rectangular). The differential technique utilizes two bar-shaped samples, glued orthogonal to each other (top), the modified Montgomery technique uses a single square sample, with four contacts on the corner (middle), and the transverse technique uses on a five-contact bar-shaped sample rotated 45° with respect to the poling direction of the piezostack (bottom). The red arrow shows the crystal axis for each configuration. (b)–(e) Representative data of the resistivity as a function of strain in the isotropic A_{1g} and anisotropic E_{2g} channels at several temperatures measured by the modified Montgomery technique. (f) The temperature dependence of elastoresistivity coefficients measured by the modified Montgomery technique. The black dashed line represents T_{CDW}, and the gray dashed line indicates T^*. (g) The temperature dependence of $m_{A_{1g}}$ measured by three techniques. (h) The same plot as (g) for $m_{E_{2g}}$.

regime. Figure 2(f) shows the temperature dependence of E_{2g} and A_{1g} elastoresistivity coefficients measured by the modified Montgomery technique. The $m_{E_{2g}}$ value jumps from 3 to 8 at T_{CDW}, but it is essentially temperature independent both below and above T_{CDW}. The $m_{A_{1g}}$ is also temperature independent above T_{CDW}, albeit with a larger value (approximately 10). At T_{CDW}, it exhibits a sharp peak and grows continuously as temperature decreases until reaching a maximum value of 90 at $T^* = 20$ K.

The $m_{E_{2g}}$ measured by the modified Montgomery technique is very different from those reported in Refs. [40,41], which were measured by the differential elastoresistivity technique. The $m_{E_{2g}}$ reported in Refs. [40,41] is considerably larger and shows a temperature dependence that resembles $m_{A_{1g}}$ measured by the modified Montgomery technique. To gain more insight, we present the elastoresistivity coefficients measured by all three techniques in Figs. 2(g) and 2(h). It can be seen that $m_{E_{2g}}$ and $m_{A_{1g}}$ measured by the modified Montgomery technique and the

transverse technique are consistent with each other, whereas the differential elastoresistivity technique yields a larger $m_{E_{2g}}$ and smaller $m_{A_{1g}}$ in comparison to the other two techniques. The temperature dependence of $m_{E_{2g}}$ measured by the differential elastoresistivity technique is also more similar to that of $m_{A_{1g}}$. All of these are consistent with the admixture of $m_{A_{1g}}$ into $m_{E_{2g}}$ in the differential elastoresistivity measurement due to unequal strain transmission in the two samples. Hence, we conclude that the divergent $m_{E_{2g}}$ in previous reports is not intrinsic. We note that two groups have also reported elastoresistivity measurements during the preparation of this manuscript, which are in broad agreement with our observations [64,65]. A detailed comparison of the results among different groups is discussed in Supplemental Material [66].

C. Elastocaloric effect

In addition to the elastoresistivity measurements, the elastocaloric effect (ECE) is another sensitive probe to

measure the diverging susceptibility associated with a nematic phase transition [67,68]. The elastocaloric measurement detects the temperature change of a system due to an adiabatically induced strain. Experimentally, a small ac strain is induced in the sample simultaneously with a tunable dc bias strain, and the ac temperature variation is measured at the frequency of the induced strain by a thermocouple (see details in Sec. V). The elastocaloric coefficient ($\partial T/\partial \varepsilon$) can be related to the isothermal entropy change caused by strain via the following equation:

$$\left(\frac{\partial T}{\partial \varepsilon}\right)_S = -\frac{T}{C_\varepsilon}\left(\frac{\partial S}{\partial \varepsilon}\right)_T, \tag{2}$$

where C_ε is the heat capacity at a given strain and S is entropy. The elastocaloric effect is sensitive to both the susceptibility of the nematic order parameter as well as its spontaneous onset. Depending on the symmetry of the induced strain, two ECE phenomena are expected near a phase transition [68,69], the first of which is associated with inducing strain that breaks the same symmetry as the order parameter [68]. When using such a strain to perturb the system, an enhancement of ECE above the transition temperature is expected. This enhanced ECE is described by the following equation:

$$\left(\frac{\partial T}{\partial \varepsilon_i}\right)_S = -\frac{T\lambda^2\varepsilon_i}{C_{\varepsilon_i}}\left(\frac{d\chi_N}{dT}\right), \tag{3}$$

where i labels the anisotropic symmetry channels. Thus, this enhancement of the ECE is proportional to both the temperature derivative of the susceptibility ($d\chi_N/dT$) and the dc bias anisotropic strain ε_i; hence, it switches sign from tensile to compressive dc strain. This effect was observed in the iron-based superconductors where $\varepsilon_{B_{2g}}$ couples linearly to electronic nematicity and showed excellent agreement with the nematic susceptibility obtained from previous elastoresistivity measurements [68,70].

The second effect is associated with the temperature shift of the phase transition induced by strains with symmetry that do *not* couple linearly to the order parameter. For example, $\varepsilon_{A_{1g}}$ is expected to linearly tune T_{CDW}. In this case, we expect the ECE near the phase transition to be proportional to the critical contribution of heat capacity ($C^{(c)}_{\varepsilon_{E_{2g}}}$) times the strain derivative of transition temperature:

$$\left(\frac{\partial T}{\partial \varepsilon_{A_{1g}}}\right)_S = \frac{C^{(c)}_{\varepsilon_{E_{2g}}}}{C_{\varepsilon_{E_{2g}}}}\frac{dT_{CDW}}{d\varepsilon_{A_{1g}}}. \tag{4}$$

We measured the ECE of a CsV_3Sb_5 sample by applying a uniaxial stress, which induces both $\varepsilon_{A_{1g}}$ and $\varepsilon_{E_{2g}}$. Figure 3(a) summarizes the ECE measured under different dc bias strains. A pronounced peak that mimics the heat capacity

anomaly is observed near T_{CDW}, and the peak is systematically shifted as a function of dc bias strain. This peak is consistent with the second effect mentioned above, where $\varepsilon_{A_{1g}}$ linearly shifts the transition temperature. The linear dependence of T_{CDW} as a function of A_{1g} strain is also consistent with previous studies of CsV_3Sb_5 [71].

However, the enhancement of the ECE due to a diverging nematic susceptibility was not observed either above or below T_{CDW}. The signal quickly converges both above and below T_{CDW} [Fig. 3(b)], and there is no indication of concavity or slope change in the peak from tensile to compressive strains. This result is consistent with no diverging nematic susceptibility, further corroborating the conclusion established by the elastoresistivity measurements. A very recent study suggested an odd-parity nematic transition above T_{CDW} which turns into a first-order transition under a c-axis magnetic field [65]. We also performed ECE measurements under a c-axis magnetic
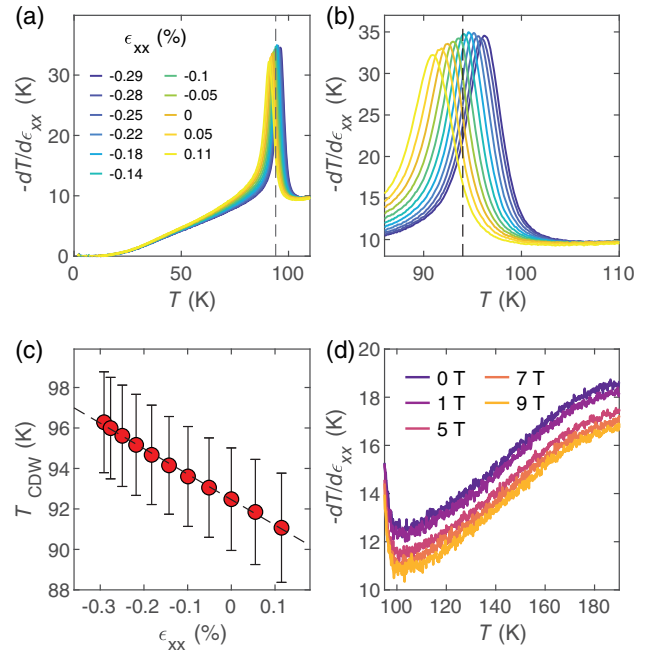

FIG. 3. ac elastocaloric effect. (a) Temperature dependence of the ECE measured at different dc bias uniaxial strains. The uniaxial stress was applied along the longitudinal direction of a bar-shaped sample cut along the a axis. The data were taken at a 1 K/min cooling rate. (b) An enlarged view of the peaks in ECE near T_{CDW}. (c) The CDW transition temperature as a function of strain determined by the peaks in ECE at T_{CDW}. The error bar is determined by the full width at half maximum of the peaks. The dashed line represents a linear fit to $T_{CDW}(\varepsilon)$ with a slope of $dT_{CDW}/d\varepsilon_{xx} = -12.6$ K/%. (d) ECE data above the CDW transition under various magnetic fields measured in a different sample. The magnetic field is along the c axis, and the dc-biased strain is near zero. There is no change of ECE signal as a function of the magnetic field except for a slight shift of the background due to the weak field dependence of the voltage response of a type-E thermocouple above 100 K [72].

field up to 9 T and observed no anomaly above T_{CDW} as illustrated in Fig. 3(d). This result is consistent with the absence of such a transition measured by thermal expansion experiments [64].

III. DISCUSSION

Both elastoresistivity and elastocaloric effect measurements suggest the absence of the nematic instability below T_{CDW}. The diverging $m_{E_{2g}}$ reported in Refs. [40,41] is most likely due to the mixing of the diverging $m_{A_{1g}}$, a consequence of unequal strain transmissions in the differential elastoresistivity technique. We note that, in Ref. [41], the Montgomery elastoresistivity measurement was performed on one Ti-doped CsV_3Sb_5 sample, which showed agreement with the differential elastoresistivity measurement. Given that the unequal strain transmission is a generic issue in all differential elastoresistivity measurements, a reinvestigation of the elastoresistivity of Ti-doped CsV_3Sb_5 is highly warranted.

We also note that our result is not inconsistent with the rotational symmetry breaking at T_{CDW}. The increase of $m_{E_{2g}}$ could be a result of aligning symmetry-breaking CDW domains by the anisotropic strain [22,32,73], but the small value of $m_{E_{2g}}$ (approximately 8) indicates that the electronic anisotropy is only moderately larger than the structural anisotropy [74], which could be consistent with the weak anisotropy introduced by the interlayer coupling. In this scenario, given that both rotational symmetry and translational symmetry are simultaneously broken at T_{CDW}, this transition cannot be characterized as a nematic transition. The absence of diverging E_{2g} elastoresistivity and elastocaloric effect above T_{CDW} also confirms that there is no fluctuating vestigial nematicity associated with the rotational symmetry-breaking CDW. The temperature-independent E_{2g} elastoresistivity also suggests that the previously reported $4a_0$ order observed by STM is likely a surface phenomenon, which does not contribute to bulk electronic anisotropy [10,12]. Instead of diverging $m_{E_{2g}}$, the dominant response is in the isotropic A_{1g} channel, manifested by the diverging $m_{A_{1g}}$. Below, we discuss the possible origins of the large and strongly temperature-dependent $m_{A_{1g}}$. There are two features in the temperature dependence of $m_{A_{1g}}$. The first feature is a sharp peak at T_{CDW}, which can be understood by the generalized Fisher-Langer relation [69]. The relation states that the temperature derivative of resistivity, $d\rho/dT$, the ECE, and elastoresistivity coefficient all scale like the critical component of the heat capacity near a phase transition, if the strain used in the ECE and elastoresistivity is associated with the same symmetry channel that is orthogonal to the order parameter. Indeed, as shown in Fig. 4(a), all three quantities follow the same temperature dependence near T_{CDW}. As a side note, this phenomenon can appear in the $m_{E_{2g}}$ channel as well, if the sample is at a
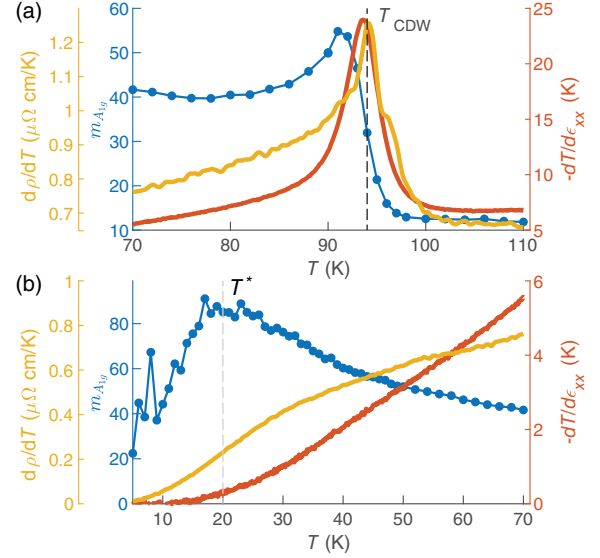

FIG. 4. Comparison of $m_{A_{1g}}$, ECE, and $d\rho/dT$ in CsV_3Sb_5. Temperature dependence of $m_{A_{1g}}$ (blue points), $-dT/d\varepsilon_{xx}$ at zero strain (red line), and $d\rho/dT$ (yellow line) are plotted near T_{CDW} (vertical dashed line) (a) and in the low-temperature range (b). The vertical gray dashed line indicates T^*.

nonzero E_{2g} strain, since T_{CDW} is potentially a quadratic function of $\epsilon_{E_{2g}}$.

Below T_{CDW}, the $m_{A_{1g}}$ increases rapidly as temperature decreases, showing a diverging behavior that peaks at T^*. In contrast to the sharp peak at T_{CDW}, we do not see similar temperature dependence in the ECE, and $d\rho/dT$ shows only a broad hump centered at T^* that barely resembles the feature in $m_{A_{1g}}$ [Fig. 4(b)]. The lack of any feature in the ECE and the strong divergence in elastoresistivity is rather striking. If we attribute the divergence of $m_{A_{1g}}$ to a phase transition at T^*, it implies that the order parameter has a very weak coupling to strain, such that it causes a minimum entropy change induced by strain, yet it has a very strong coupling to the conducting quasiparticles, leading to the strong divergence in elastoresistivity. This phenomenon has been observed in iron-based superconductors, where the magnitude of ECE decreases by factor of 35 as the doping approaches the nematic quantum critical point, while the elastoresistivity is enhanced by fivefold [68]. It was understood as a consequence of simultaneous reduction of nematoelastic coupling and enhancement of nematotransport coupling.

Another notable observation is that the temperature dependence of $m_{A_{1g}}$ shows a striking resemblance to that of the AHE discovered in the CDW phase of the AV_3Sb_5 family [3,19,20], since the temperature dependence of $m_{A_{1g}}$ can be decomposed into two components: a peak near T_{CDW} that resembles $d\rho/dT$ and a diverging behavior toward T^*. To isolate diverging behavior toward T^*, we normalized both $m_{A_{1g}}$ and $d\rho/dT$ [Fig. 5(a)] and subtract
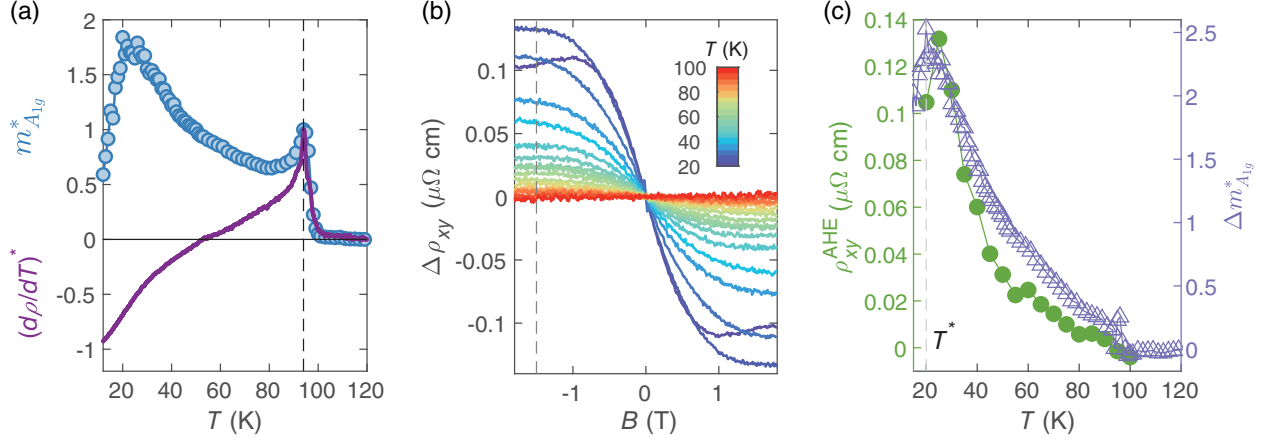
FIG. 5. Similarity between the temperature dependence of AHE and $m_{A_{1g}}$. (a) Temperature dependence of elastoresistivity $m_{A_{1g}}$ and the temperature derivative of resistivity normalized by the peak value at T_{CDW}. The elastoresistivity $m_{A_{1g}}$ was subtracted by a temperature-independent background (its value at 120 K, $m_{A_{1g}}^{120\,K}$) and normalized by its peak value at T_{CDW}, i.e., $m_{A_{1g}}^* = (m_{A_{1g}} - m_{A_{1g}}^{120\,K})/(m_{A_{1g}}^{T_{CDW}} - m_{A_{1g}}^{120\,K})$. The same procedure was applied to $d\rho/dT$ to obtain $(d\rho/dT)^*$. We shifted $m_{A_{1g}}^*$ by 3 K because of the change of T_{CDW} due to thermal built-in strain. (b) $\Delta\rho_{xy}$ extracted by subtracting the linear ordinary Hall background at various temperatures (see details in Supplemental Material [66]). The black dashed line is located at -1.5 T, where we extracted the ρ_{xy}^{AHE} values. (c) ρ_{xy}^{AHE} and $\Delta m_{A_{1g}}^*$ as a function of the temperature, where $\Delta m_{A_{1g}}^* = m_{A_{1g}}^* - (d\rho/dT)^*$. This presents the temperature dependence of $m_{A_{1g}}$ without the peak feature.

the latter from the former. The anomalous Hall resistivity was extracted by removing the ordinary Hall from the ρ_{xy} in Fig. 1(c) by linearly fitting the data for fields between 1.5 and 2 T, shown in Fig. 5(b). The extracted ρ_{xy}^{AHE} as a function of the temperature is plotted against the background-subtracted $\Delta m_{A_{1g}}^*$, shown in Fig. 5(c). The remarkable resemblance of these transport observables highlights the impact of the T^* instability on the quasiparticles at the Fermi level. We notice that the recently observed chiral transport effect in CsV_3Sb_5 also shows a similar temperature dependence to AHE [25]. Intriguingly, while the AHE and the chiral transport effect are sensitive to time-reversal symmetry and inversion symmetry breaking, respectively, the A_{1g} elastoresistivity is not a direct probe of either symmetry-breaking order parameters, because both resistivity and strain are even-parity operators. Future studies on the strain dependence of AHE and nonlinear transport effect may elucidate the origin of the common diverging behavior of all three transport observables. There has also been a suggestion that the small Fermi pockets observed in quantum oscillations may be relevant to AHE or field-tunable chirality [11,24–26]. This may also be resolved by performing strain-dependent quantum oscillation measurements.

IV. CONCLUSION

In summary, we investigated the isotropic and anisotropic elastoresistivity coefficients $m_{A_{1g}}$ and $m_{E_{2g}}$, as well as the elastocaloric effect in CsV_3Sb_5. The lack of enhancement in elastocaloric effect and the temperature-

independent $m_{E_{2g}}$ below T_{CDW} are both consistent with the absence of nematic instability in this system. The previously reported diverging elastoresistivity $m_{E_{2g}}$ is likely due to the cross-contamination from $m_{A_{1g}}$. Both the elastoresistivity coefficient $m_{A_{1g}}$ and the ECE show a peak at T_{CDW}, which is a consequence of the tuning of T_{CDW} by A_{1g} strain, and it is consistent with the extended Fisher-Langer relation. In addition to the peak at T_{CDW}, $m_{A_{1g}}$ also shows a diverging temperature dependence below T_{CDW} that reaches a maximum at T^*, but there is no corresponding elastocaloric anomaly. Our results show that there is no nematic phase transition within the CDW phase in CsV_3Sb_5, and the nature of T^* requires further investigation.

V. METHODS

A. Transport measurements

Single crystals of CsV_3Sb_5 were synthesized using a self-flux method described elsewhere [7,71,75]. The electrical transport measurements were performed in DynaCool (Quantum Design, Inc.). The high magnetic field experiments were carried out in a 35 T resistive magnet at the National High Magnetic Field Laboratory in Tallahassee, Florida.

B. Elastoresistivity tensor in D_{6h} point group

The symmetry decomposition of elastoresistivity tensor in the D_{6h} point group is different from that in D_{4h}. There are two irreducible representations in D_{6h} that are relevant to this study: isotropic A_{1g} and anisotropic

E_{2g} symmetry. The in-plane biaxial strain employed in this study can be decomposed into these two symmetry channels: $\varepsilon_{A_{1g,1}} = (\varepsilon_{xx} + \varepsilon_{yy})/2$, $\varepsilon_{A_{1g,2}} = \varepsilon_{zz}$, and $\varepsilon_{E_{2g}} = [(\varepsilon_{xx} - \varepsilon_{yy})/2, \varepsilon_{xy}]$. We note that E_{2g} is a two-dimensional irreducible representation and $(\varepsilon_{xx} - \varepsilon_{yy})/2$ and ε_{xy} are the two bases. The in-plane resistivity tensors can also be decomposed into these two irreducible representations:

$$(\Delta\rho/\rho)_{A_{1g,1}} = \frac{1}{2}[(\Delta\rho/\rho)_{xx} + (\Delta\rho/\rho)_{yy}],$$
$$(\Delta\rho/\rho)_{A_{1g,2}} = (\Delta\rho/\rho)_{zz},$$
$$(\Delta\rho/\rho)_{E_{2g}} = \left\{\frac{1}{2}[(\Delta\rho/\rho)_{xx} - (\Delta\rho/\rho)_{yy}], (\Delta\rho/\rho)_{xy}\right\}. \quad (5)$$

Therefore, if we focus on the in-plane elastoresistivity, coefficients in isotropic A_{1g} and anisotropic E_{2g} symmetry channels are related to the elastoresistivity tensors in the Cartesian coordinate systems by the following expressions:

$$m_{A_{1g}} = \frac{(\Delta\rho/\rho)_{A_{1g}}}{\varepsilon_{A_{1g}}}$$
$$= \frac{(m_{xx,xx} + m_{xx,yy})(\varepsilon_{xx} + \varepsilon_{yy}) + 2m_{xx,zz}\varepsilon_{zz}}{\varepsilon_{xx} + \varepsilon_{yy}}$$
$$= m_{xx,xx} + m_{xx,yy} - m_{xx,zz}\left(\frac{2\nu_{ac}}{1 - \nu_{ab}}\right),$$
$$m_{E_{2g}} = \frac{(\Delta\rho/\rho)_{E_{2g}}}{\varepsilon_{E_{2g}}}$$
$$= \frac{(m_{xx,xx} - m_{xx,yy})(\varepsilon_{xx} - \varepsilon_{yy})}{\varepsilon_{xx} - \varepsilon_{yy}}$$
$$= m_{xx,xx} - m_{xx,yy}. \quad (6)$$

Since the sample is glued down to the side wall of the piezostack by the Stycast, its in-plane deformation will be constrained by the deformation of the piezostacks. Consequently, $\nu_{ab} = -\epsilon_{yy}/\epsilon_{xx}$ and $\nu_{ac} = -\epsilon_{zz}/\epsilon_{xx}$ are the Poisson ratios of the piezostacks and the sample, respectively. We note that, because E_{2g} is a two-dimensional irreducible representation, $m_{E_{2g}} = m_{xy,xy} = m_{xx,xx} - m_{xx,yy}$. In Voigt notation, $1 = xx$, and $2 = yy$; hence, $m_{A_{1g}} = m_{11} + m_{12} - m_{13}[2\nu_{ac}/(1 - \nu_{ab})]$ and $m_{E_{2g}} = m_{11} - m_{12}$.

C. Elastoresistivity techniques

A tunable strain was applied to single crystal samples by gluing them on the sidewall of a piezostack (P-885.11, from PI-USA) using a thermally conductive epoxy (Stycast 2850FT with Catalyst 24LV, from Loctite). The uniaxial strain along the poling direction of the piezostack, ε_{yy} [Fig. 2(a)], was measured by a foil strain gauge (CEA-06-062UWA-350, from Micro-Measurements), which was glued to the other side of the piezostack. The uniaxial

strain along the orthogonal direction, ε_{xx}, was determined by the known in-plane Poisson ratio of the piezostack. As discussed in the main text, the elastoresistivity coefficients can be measured by three techniques.

(i) *Differential technique.*—Two bar-shaped samples are glued to the piezostack. The bar directions are aligned with the transverse and poling directions of the piezostack. Using the standard four-terminal technique, the resistivity ρ_{xx} and ρ_{yy} are measured separately in each sample.

(ii) *Modified Montgomery technique.*—Four electric contacts are made at the corners of a square-shaped sample, which is glued on the piezostack with the edges aligned to the poling direction. R_{xx} and R_{yy} are measured by sourcing current using the contacts on one side and measuring the voltage using the contacts on the other side. The measured resistance R_{xx} and R_{yy} can then be converted to resistivity ρ_{xx} and ρ_{yy} following the procedure in Supplemental Material [66].

(iii) *Transverse technique.*—The transverse technique measures the transverse resistivity ρ_{xy} induced by shear strain ε_{xy}, which is different from the other two techniques that measures the longitudinal resistivity ρ_{xx} and ρ_{yy} [63]. The shear strain ε_{xy} is equivalent to an anisotropic strain $(\varepsilon_{xx} - \varepsilon_{yy})/2$ under 45° rotation. In the transverse technique, a Hall bar with five electrical contacts is glued onto the piezostack and is aligned at a 45° angle with respect to the y axis. Note that there is no magnetic field; hence, the transverse resistivity ρ_{xy} is not a result of the Hall effect.

The main problem with the differential technique is the contamination of the isotropic strain channel to other anisotropic channels due to unequal strain transmission between two samples. This effect is inevitable as long as the samples are cut into bar shape and glued along orthogonal directions [45,63]. This effect becomes crucial when the elastoresistivity coefficient in the isotropic channel is much larger than the anisotropic channel. In this respect, both modified Montgomery and transverse techniques can perfectly eliminate this effect by measuring a single sample.

D. Elastocaloric effect measurement

The elastocaloric effect was measured using an ac (dynamic) ECE technique with a homemade three-piezo-stack uniaxial strain cell, similar to the piezoelectric strain cell developed by Hicks *et al.* [76]. The sample was glued across the gap of the sample mounts of the strain cell. The temperature of the sample was measured at the center of the sample using a Chromel-AuFe0.07% (25 μm wire diameter) or type-E thermocouple for lower or higher temperature range, respectively. To apply a dynamical strain together with a static offset, ac and dc voltages were applied to the piezostacks using a TEGAM 2350 high-voltage amplifier

sourced by a Stanford Research SR860 Lock-in amplifier and Keithley 2450 voltage supply, respectively. The signals from the sample and thermocouple were amplified by the Stanford Research SR554 preamplifier and measured by SR860. We present the thermal transfer function and phase as a function of frequency in Fig. S5 in Supplemental Material [66]. Accordingly, we set the frequency 25.5 Hz to achieve the quasiadiabatic condition in our measurements. The details of the ac ECE technique can be found in Refs. [67,68,70].

ACKNOWLEDGMENTS

---

[1] T. Neupert, M. M. Denner, J. X. Yin, R. Thomale, and M. Z. Hasan, *Charge order and superconductivity in kagome materials*, Nat. Phys. **18**, 137 (2022).

[2] H.-M. Guo and M. Franz, *Topological insulator on the kagome lattice*, Phys. Rev. B **80**, 113102 (2009).

[3] E. Liu *et al.*, *Giant anomalous Hall effect in a ferromagnetic kagome-lattice semimetal*, Nat. Phys. **14**, 1125 (2018).

[4] L. Ye *et al.*, *Massive Dirac fermions in a ferromagnetic kagome metal*, Nature (London) **555**, 638 (2018).

[5] H. W. S. Arachchige, W. R. Meier, M. Marshall, T. Matsuoka, R. Xue, M. A. McGuire, R. P. Hermann, H. Cao, and D. Mandrus, *Charge density wave in kagome lattice intermetallic* ScV_6Sn_6, Phys. Rev. Lett. **129**, 216402 (2022).

[6] X. Teng *et al.*, *Discovery of charge density wave in a kagome lattice antiferromagnet*, Nature (London) **609**, 490 (2022).

[7] B. R. Ortiz *et al.*, CsV_3Sb_5: *A* Z_2 *topological kagome metal with a superconducting ground state*, Phys. Rev. Lett. **125**, 247002 (2020).

[8] B. R. Ortiz *et al.*, *New kagome prototype materials: Discovery of* KV_3Sb_5, RbV_3Sb_5, *and* CsV_3Sb_5, Phys. Rev. Mater. **3**, 094407 (2019).

[9] Z. Liang *et al.*, *Three-dimensional charge density wave and surface-dependent vortex-core states in a kagome superconductor* CsV_3Sb_5, Phys. Rev. X **11**, 031026 (2021).

[10] H. Zhao, H. Li, B. R. Ortiz, S. M. L. Teicher, T. Park, M. Ye, Z. Wang, L. Balents, S. D. Wilson, and I. Zeljkovic, *Cascade of correlated electron states in the kagome superconductor* CsV_3Sb_5, Nature (London) **599**, 216 (2021).

[11] Y.-X. Jiang *et al.*, *Unconventional chiral charge order in kagome superconductor* KV_3Sb_5, Nat. Mater. **20**, 1353 (2021).

[12] H. Li *et al.*, *Discovery of conjoined charge density waves in the kagome superconductor* CsV_3Sb_5, Nat. Commun. **13**, 6348 (2022).

[13] Q. Xiao *et al.*, *Coexistence of multiple stacking charge density waves in kagome superconductor* CsV_3Sb_5, Phys. Rev. Res. **5**, L012032 (2023).

[14] K. Jiang, T. Wu, J.-X. Yin, Z. Wang, M. Z. Hasan, S. D. Wilson, X. Chen, and J. Hu, *Kagome superconductors* AV_3Sb_5 *(A = K, Rb, Cs)*, Natl. Sci. Rev. **10**, nwac199 (2023).

[15] H. Li *et al.*, *Observation of unconventional charge density wave without acoustic phonon anomaly in kagome superconductors* AV_3Sb_5 *(A = Rb, Cs)*, Phys. Rev. X **11**, 031050 (2021).

[16] Y. Xie *et al.*, *Electron-phonon coupling in the charge density wave state of* CsV_3Sb_5, Phys. Rev. B **105**, L140501 (2022).

[17] M. H. Christensen, T. Birol, B. M. Andersen, and R. M. Fernandes, *Theory of the charge density wave in* AV_3Sb_5 *kagome metals*, Phys. Rev. B **104**, 214513 (2021).

[18] S. D. Wilson and B. R. Ortiz, AV_3Sb_5 *kagome superconductors*, Nat. Rev. Mater. **9**, 420 (2024).

[19] S. Y. Yang *et al.*, *Giant, unconventional anomalous Hall effect in the metallic frustrated magnet candidate,* KV_3Sb_5, Sci. Adv. **6**, 1 (2020).

[20] F. H. Yu, T. Wu, Z. Y. Wang, B. Lei, W. Z. Zhuo, J. J. Ying, and X. H. Chen, *Concurrence of anomalous Hall effect and charge density wave in a superconducting topological kagome metal*, Phys. Rev. B **104**, L041103 (2021).

[21] L. Yu *et al.*, *Evidence of a hidden flux phase in the topological kagome metal* CsV_3Sb_5, arXiv:2107.10714.

[22] Y. Xu *et al.*, *Three-state nematicity and magneto-optical Kerr effect in the charge density waves in kagome superconductors*, Nat. Phys. **18**, 1470 (2022).

[23] C. Mielke *et al.*, *Time-reversal symmetry-breaking charge order in a kagome superconductor*, Nature (London) **602**, 245 (2022).

[24] D. Chen *et al.*, *Anomalous thermoelectric effects and quantum oscillations in the kagome metal* CsV_3Sb_5, Phys. Rev. B **105**, L201109 (2022).

[25] C. Guo *et al.*, *Switchable chiral transport in charge-ordered kagome metal* CsV_3Sb_5, Nature (London) **611**, 461 (2022).

[26] Y. Xing *et al.*, *Optical manipulation of the charge-density-wave state in* RbV_3Sb_5, Nature (London) **631**, 60 (2024).

[27] X. Feng, Y. Zhang, K. Jiang, and J. Hu, *Low-energy effective theory and symmetry classification of flux phases on the kagome lattice*, Phys. Rev. B **104**, 165136 (2021).

[28] M. H. Christensen, T. Birol, B. M. Andersen, and R. M. Fernandes, *Loop currents in* AV_3Sb_5 *kagome metals: Multipolar and toroidal magnetic orders*, Phys. Rev. B **106**, 144504 (2022).

[29] D. R. Saykin *et al.*, *High resolution polar Kerr effect studies of* CsV_3Sb_5*: Tests for time-reversal symmetry breaking below the charge-order transition*, Phys. Rev. Lett. **131**, 016901 (2023).

[30] J. Wang, C. Farhang, B. R. Ortiz, S. D. Wilson, and J. Xia, *Resolving the discrepancy between moke measurements at 1550-nm wavelength on kagome metal* CsV_3Sb_5, Phys. Rev. Mater. **8**, 014202 (2024).

[31] Y. Xiang *et al.*, *Twofold symmetry of c-axis resistivity in topological kagome superconductor* CsV_3Sb_5 *with in-plane rotating magnetic field*, Nat. Commun. **12**, 6727 (2021).

[32] H. Li *et al.*, *Rotation symmetry breaking in the normal state of a kagome superconductor* KV_3Sb_5, Nat. Phys. **18**, 265 (2022).

[33] H. Li *et al.*, *Unidirectional coherent quasiparticles in the high-temperature rotational symmetry broken phase of* AV_3Sb_5 *kagome superconductors*, Nat. Phys. **19**, 637 (2023).

[34] D. Wulferding *et al.*, *Emergent nematicity and intrinsic versus extrinsic electronic scattering processes in the kagome metal* CsV_3Sb_5, Phys. Rev. Res. **4**, 023215 (2022).

[35] S. Wu, B. R. Ortiz, H. Tan, S. D. Wilson, B. Yan, T. Birol, and G. Blumberg, *Charge density wave order in the kagome metal* AV_3Sb_5 *(A = Cs, Rb, K)*, Phys. Rev. B **105**, 155106 (2022).

[36] Q. Wu *et al.*, *Simultaneous formation of two-fold rotation symmetry with charge order in the kagome superconductor* CsV_3Sb_5 *by optical polarization rotation measurement*, Phys. Rev. B **106**, 205109 (2022).

[37] Z. Jiang *et al.*, *Observation of electronic nematicity driven by the three-dimensional charge density wave in kagome lattice* KV_3Sb_5, Nano Lett. **23**, 5625 (2023).

[38] H. Luo *et al.*, *Electronic nature of charge density wave and electron-phonon coupling in kagome superconductor* KV_3Sb_5, Nat. Commun. **13**, 273 (2022).

[39] M. Kang *et al.*, *Charge order landscape and competition with superconductivity in kagome metals*, Nat. Mater. **22**, 186 (2023).

[40] L. Nie *et al.*, *Charge-density-wave-driven electronic nematicity in a kagome superconductor*, Nature (London) **604**, 59 (2022).

[41] Y. Sur, K.-T. Kim, S. Kim, and K. H. Kim, *Optimized superconductivity in the vicinity of a nematic quantum critical point in the kagome superconductor* $Cs(V_{1-x}Ti_x)_3Sb_5$, Nat. Commun. **14**, 3899 (2023).

[42] E. Fradkin, S. A. Kivelson, M. J. Lawler, J. P. Eisenstein, and A. P. Mackenzie, *Nematic fermi fluids in condensed matter physics*, Annu. Rev. Condens. Matter Phys. **1**, 153 (2010).

[43] R. Fernandes, A. Chubukov, and J. Schmalian, *What drives nematic order in iron-based superconductors?*, Nat. Phys. **10**, 97 (2014).

[44] J.-H. Chu, H.-H. Kuo, J. G. Analytis, and I. R. Fisher, *Divergent nematic susceptibility in an iron arsenide superconductor*, Science **337**, 710 (2012).

[45] H.-H. Kuo, J.-H. Chu, J. C. Palmstrom, S. A. Kivelson, and I. R. Fisher, *Ubiquitous signatures of nematic quantum criticality in optimally doped Fe-based superconductors*, Science **352**, 958 (2016).

[46] Z. Liu *et al.*, *Nematic quantum critical fluctuations in* $BaFe_{2-x}Ni_xAs_2$, Phys. Rev. Lett. **117**, 157002 (2016).

[47] Y. Gu *et al.*, *Unified phase diagram for iron-based superconductors*, Phys. Rev. Lett. **119**, 157001 (2017).

[48] L. Nie, G. Tarjus, and S. A. Kivelson, *Quenched disorder and vestigial nematicity in the pseudogap regime of the cuprates*, Proc. Natl. Acad. Sci. U.S.A. **111**, 7980 (2014).

[49] R. M. Fernandes, P. P. Orth, and J. Schmalian, *Intertwined vestigial order in quantum materials: Nematicity and beyond*, Annu. Rev. Condens. Matter Phys. **10**, 133 (2019).

[50] A. E. Böhmer, J.-H. Chu, S. Lederer, and M. Yi, *Nematicity and nematic fluctuations in iron-based superconductors*, Nat. Phys. **18**, 1412 (2022).

[51] T. Park, M. Ye, and L. Balents, *Electronic instabilities of kagome metals: Saddle points and Landau theory*, Phys. Rev. B **104**, 035142 (2021).

[52] F. Grandi, A. Consiglio, M. A. Sentef, R. Thomale, and D. M. Kennes, *Theory of nematic charge orders in kagome metals*, Phys. Rev. B **107**, 155131 (2023).

[53] M. M. Denner, R. Thomale, and T. Neupert, *Analysis of charge order in the kagome metal* AV_3Sb_5 *(A = K, Rb, Cs)*, Phys. Rev. Lett. **127**, 217601 (2021).

[54] R. Tazai, Y. Yamakawa, S. Onari, and H. Kontani, *Mechanism of exotic density-wave and beyond-Migdal unconventional superconductivity in kagome metal* AV_3Sb_5 *(A = K, Rb, Cs)*, Sci. Adv. **8**, eabl4108 (2022).

[55] S. Zhou and Z. Wang, *Chern Fermi pocket, topological pair density wave, and charge-4e and charge-6e superconductivity in kagomé superconductors*, Nat. Commun. **13**, 7288 (2022).

[56] P. Wiecki, A. A. Haghighirad, F. Weber, M. Merz, R. Heid, and A. E. Bohmer, *Dominant in-plane symmetric elastoresistance in* $CsFe_2As_2$, Phys. Rev. Lett. **125**, 187001 (2020).

[57] P. Wiecki *et al.*, *Emerging symmetric strain response and weakening nematic fluctuations in strongly hole-doped iron-based superconductors*, Nat. Commun. **12**, 4824 (2021).

[58] E. W. Rosenberg, J.-H. Chu, J. P. Ruff, A. T. Hristov, and I. R. Fisher, *Divergence of the quadrupole-strain susceptibility of the electronic nematic system* $YbRu_2Ge_2$, Proc. Natl. Acad. Sci. U.S.A. **116**, 7232 (2019).

[59] L. Ye *et al.*, *Elastocaloric signatures of symmetric and antisymmetric strain-tuning of quadrupolar and magnetic phases in* DyB_2C_2, Proc. Natl. Acad. Sci. U.S.A. **120**, e2302800120 (2023).

[60] B. R. Ortiz, S. M. L. Teicher, L. Kautzsch, P. M. Sarte, N. Ratcliff, J. Harter, J. P. C. Ruff, R. Seshadri, and S. D. Wilson, *Fermi surface mapping and the nature of charge density wave order in the kagome superconductor* CsV_3Sb_5, Phys. Rev. X **11**, 041030 (2021).

[61] Y. Fu *et al.*, *Quantum transport evidence of topological band structures of kagome superconductor* CsV_3Sb_5, Phys. Rev. Lett. **127**, 207002 (2021).

[62] R. M. Fernandes and J. W. Venderbos, *Nematicity with a twist: Rotational symmetry breaking in a moiré superlattice*, Sci. Adv. **6**, eaba8834 (2020).

[63] M. Shapiro, A. Hristov, J. Palmstrom, J.-H. Chu, and I. Fisher, *Measurement of the* B_{1g} *and* B_{2g} *components of the elastoresistivity tensor for tetragonal materials via transverse resistivity configurations*, Rev. Sci. Instrum. **87**, 063902 (2016).

[64] M. Frachet *et al.*, *Colossal c-axis response and lack of rotational symmetry breaking within the kagome planes of the* CsV_3Sb_5 *superconductor*, Phys. Rev. Lett. **132**, 186001 (2024).

[65] T. Asaba *et al.*, *Evidence for an odd-parity nematic phase above the charge-density-wave transition in a kagome metal*, Nat. Phys. **20**, 40 (2024).

[66] See Supplemental Material at http://link.aps.org/supplemental/10.1103/PhysRevX.14.031015 for experimental details of elastoresistivity and elastocaloric effect measurements.

[67] M. S. Ikeda *et al.*, *AC elastocaloric effect as a probe for thermodynamic signatures of continuous phase transitions*, Rev. Sci. Instrum. **90**, 083902 (2019).

[68] M. S. Ikeda *et al.*, *Elastocaloric signature of nematic fluctuations*, Proc. Natl. Acad. Sci. U.S.A. **118**, e2105911118 (2021).

[69] A. T. Hristov, M. S. Ikeda, J. C. Palmstrom, P. Walmsley, and I. R. Fisher, *Elastoresistive and elastocaloric anomalies at magnetic and electronic-nematic critical points*, Phys. Rev. B **99**, 100101(R) (2019).

[70] J. Straquadine, M. Ikeda, and I. Fisher, *Frequency-dependent sensitivity of ac elastocaloric effect measurements explored through analytical and numerical models*, Rev. Sci. Instrum. **91**, 083905 (2020).

[71] T. Qian, M. H. Christensen, C. Hu, A. Saha, B. M. Andersen, R. M. Fernandes, T. Birol, and N. Ni, *Revealing the competition between charge density wave and superconductivity in* CsV_3Sb_5 *through uniaxial strain*, Phys. Rev. B **104**, 144506 (2021).

[72] A. Inyushkin, K. Leicht, and P. Esquinazi, *Magnetic field dependence of the sensitivity of a type E (chromel-constantan) thermocouple*, Cryogenics **38**, 299 (1998).

[73] Q. Wu *et al.*, *Simultaneous formation of two-fold rotation symmetry with charge order in the kagome superconductor* CsV_3Sb_5 *by optical polarization rotation measurement*, Phys. Rev. B **106**, 205109 (2022).

[74] C. Guo *et al.*, *Correlated order at the tipping point in the kagome metal* CsV_3Sb_5, Nat. Phys. **20**, 579 (2024).

[75] Z. Wang *et al.*, *Electronic nature of chiral charge order in the kagome superconductor* CsV_3Sb_5, Phys. Rev. B **104**, 075148 (2021).

[76] C. W. Hicks, M. E. Barber, S. D. Edkins, D. O. Brodsky, and A. P. Mackenzie, *Piezoelectric-based apparatus for strain tuning*, Rev. Sci. Instrum. **85**, 065003 (2014).